J. Electrochem. Sci. Eng. **13(5)** (2023) 725-737; http://dx.doi.org/10.5599/jese.1595

Open Access : : ISSN 1847-9286
https://pub.iapchem.org/ojs/index.php/JESE

Original scientific paper

Vanadium oxide - poly(3,4-ethylenedioxythiophene) cathodes for zinc-ion batteries: effect of synthesis temperature*

Filipp S. Volkov, Svetlana N. Eliseeva, Mikhail A. Kamenskii, Alexey I. Volkov, Elena G. Tolstopjatova and Veniamin V. Kondratiev✉

Saint Petersburg State University, Institute of Chemistry, 7/9 Universitetskaya nab., Saint Petersburg 199034, Russia

Corresponding author: ✉vkondratiev@mail.ru; Tel.: +7-812-4286900; Fax: +7-812-4286900

Received: November 14, 2022; Accepted: February 8, 2023; Published: March 27, 2023

Abstract

Vanadium oxide composites with conducting polymer poly(3,4-ethylenedioxythiophene) (PEDOT) were obtained by one-step microwave-assisted hydrothermal synthesis at two different temperatures: 120 and 170 °C (denoted as V-120 and V-170, respectively). The structure and composition of the obtained samples were characterized by scanning electron microscopy (SEM), X-ray diffraction (XRD) analysis, X-ray photoelectron spectroscopy (XPS), and thermogravimetric (TG) analysis. The detailed study of the electrochemical properties of the composites as cathodes of aqueous zinc-ion battery was performed cyclic voltammetry (CV), galvanostatic charge-discharge (GCD) at different current densities and by electrochemical impedance spectroscopy (EIS). It was shown that V-120 demonstrated excellent electrochemical performance in the 0.3 to 1.4 V vs. *Zn/Zn^{2+} potential range reaching specific capacities up to 390 $mA{\cdot}h{\cdot}g^{-1}$ at 0.3 $A{\cdot}g^{-1}$ with excellent capacity stability after 1000 charge-discharge cycles. Its functional parameters were found to be much better than those of the electrodes based on the V-170 composite obtained at a higher temperature. The effect of the synthesis temperature on the electrochemical properties is discussed in terms of the crystallographic, compositional, and thermogravimetric properties of the samples.*

Keywords

Aqueous zinc-ion battery, hydrothermal synthesis, temperature of synthesis, electrochemical performance, structure

Introduction

The development of novel energy storage systems is at the forefront of electrochemical research. Among diverse types of metal-ion batteries, lithium-ion batteries are universally applied in various fields: electric vehicles, portable electronic devices, *etc.* [1,2]. However, a major problem of these

*Dedicated to 300th anniversary of Saint Petersburg State University

systems is unsafety due to the presence of flammable components such as electrolyte solvent or high flammability of lithium [3]. Another issue is the high cost of lithium compounds due to its low abundance. To solve these problems, other alkali-ion or multivalent metal-ion batteries such as Mg-ion, Ca-ion, Zn-ion, or Al-ion have been proposed [4-7]. Among them, aqueous zinc-ion batteries (AZIBs) have attracted increasing attention due to high gravimetric (820 $mA{\cdot}h{\cdot}g^{-1}$) and volumetric (5855 $mA{\cdot}h{\cdot}cm^{-3}$) capacities of zinc metal anode, high safety, environmental friendliness, and low cost of zinc salts [8,9].

The main problem in any metal-ion battery is the proper choice of cathode material. For AZIBs, vanadium oxides are considered as an attractive cathode due to their high reversibility towards Zn^{2+} ion intercalation, low cost and high availability, easily scalable synthesis procedures. Vanadium pentoxide V_2O_5 has the highest theoretical capacity value of 589 $mA{\cdot}h{\cdot}g^{-1}$ per two-electron transfer [10], while most reported experimental results are *ca.* 300 $mA{\cdot}h{\cdot}g^{-1}$ [11,12]. Nevertheless, the activation process for highly crystalline materials [13,14] restricts the development of commercial vanadium-based AZIBs. The activation process hinders the initial performance of the cells and results in their low cycling stability due to vanadium dissolution during both charging/discharging and storage [11,15].

To overcome these drawbacks, several solutions can be applied, *e.g.* nanostructuring of the materials, introduction of conductive additives or coatings, and substitution of vanadium ions or inclusion of different metal ions into the crystal structure of the material via pre-intercalation [16]. First, synthesis conditions can affect the crystal lattice and, in particular, the amount of crystallized water in the molecule. Water molecules can enter the crystal lattice and then be replaced by zinc ions during cycling [17-19]. It was established that the presence of water in V_6O_{13} or $V_2O_5{\cdot}nH_2O$ allows to decrease the interaction energy of zinc ions with the crystal lattice, which promotes the intercalation processes [20,21]. This can be related to the increase in interlayer spacing after water insertion [19].

Instead of carbon-modified composites which only have enhanced electronic conductivity, the use of conducting polymers allows to increase both electronic and ionic conductivities of the composite materials. The introduction of conducting polymers also improves the zinc ions diffusion within the crystal lattice because of the formation of highly porous structures and the weakening of the coulombic interactions between zinc ions and oxygen anions in the lattice, which was established for V_2O_5/polypyrrole composite [22]. Furthermore, chains or blocks of conducting polymers can enter the crystal lattice and enlarge the interlayer spacing which has been confirmed for the composites with polyaniline and its derivatives [23,24]. The use of poly(3,4-ethylenedioxythiophene) (PEDOT) enhances the electrochemical properties of vanadium oxide- [25,26], ammonium vanadate- and sodium vanadate-based electrode materials [27,28].

The incorporation of conducting polymers is usually done by two simple methods: i) *in-situ* chemical approach with partial reduction of V_2O_5 in the presence of monomer, which acts as a reductant in a reaction with solid oxidant, *i.e.* vanadium oxide species [29-31]; ii) electrochemical polymerization of a monomer to create a 3D or binder-free electrode on the conductive substrate [25]. The first method can be easily modified to obtain vanadium oxide with given morphology and polymer content. However, the effect of synthesis conditions, *e.g.* temperature, on the structural, morphological, and electrochemical properties of vanadium oxide with conducting polymer composite cathodes in AZIBs has rarely been investigated and requires further study.

In this work, the structure, composition, and electrochemical performance of vanadium oxide-based composites with PEDOT obtained at two different temperatures of microwave-assisted synthesis have been studied for the first time. It was previously reported that such a modification method resulted in superior electrochemical performance [32,33]. The effect of the temperature of

hydrothermal synthesis on the functional properties of the cathodes for aqueous zinc-ion battery was evaluated by different electrochemical techniques. The results obtained are discussed in terms of crystallographic, compositional, and thermogravimetric analyses of the synthesized products and functional properties in cathodes of AZIBs.

Experimental

Synthesis of composites

The composite materials were synthesized by soft reduction of commercial V_2O_5 (NevaReaktiv, Russia) by EDOT (97 %, Sigma-Aldrich, USA) under microwave irradiation according to the procedure adopted from [34]. The identical mixtures, consisting of 1.1 mmol of V_2O_5 and 0.42 mmol of EDOT in aqueous solution, were placed in a Pyrex reactor (35 ml). The synthesis was carried out at temperatures of 120 and 170 °C at 0.421 MPa for 1 h at 290 W microwave power level in a lab microwave system Discover SP (CEM Corp., USA). The upper limit of the temperature of 170 °C was selected as a higher temperature at which the decomposition of PEDOT did not proceed. The products were designated as V-120 and V-170. Then, the obtained dark blue powders were washed with water and ethanol, and dried at 80 °C for 2 h.

Characterization methods

The powders of the initial V_2O_5 and the composites were characterized by X-ray diffraction (XRD, D8 DISCOVER, Bruker-AXS, Germany) using Cu-K_α radiation. Scanning electron microscopy (SEM, SUPRA 40VP, Carl Zeiss, Germany) and energy dispersive X-ray analysis (EDX, Inca X-Act, Oxford Instruments, Germany) were performed on the V_2O_5 and the composite powders. After extraction of the electrodes from the cells, they were carefully rinsed with DI water and dried in air. Thermogravimetric analysis (TGA) in the 30 to 600 °C temperature range at a heating rate of 10 °C·min^{-1} in air (Netzsch TG 209 F1 Libra, Germany) was performed for the V-120 and V-170 powder samples. The X-ray photoelectron spectrometer Escalab 250Xi (Thermo Scientific, USA) equipped with an Al Kα source (photon energy of 1486.6 eV) was used to study the elemental states in the V-120 and V-170 powders, as well as in the V-120 electrode material after electrochemical studies. For comparison, in some cases, we also analyzed data for pristine V_2O_5 powder.

Electrochemical characterization

Electrode materials were prepared by mixing V-120 or V-170 with carbon black and polyvinylidene fluoride (PVDF) in a 70:20:10 weight ratio in N-methylpyrrolidone. The resulting viscous slurry was applied onto the titanium foil (current collector), vacuum-dried at 60 °C and roll-pressed. The mass loading of the electroactive material was 1.5 - 2.0 mg·cm^{-2}. Coin cells CR2032 were assembled *vs.* Zn anode with aqueous 3 mol·dm^{-3} $ZnSO_4$ (LenReactiv, Russia) as electrolyte and Whatman® glass fiber GF/A as separator.

The potentials in this work are referred to the Zn/Zn^{2+} redox couple potential. The electrochemical performance of the electrodes was studied using galvanostatic charge/discharge (GCD) and cyclic voltammetry (CV) in the 0.3 - 1.4 V potential range at 25±2 °C. Charge/discharge tests were done using a CT-4008 battery testing system (Neware Co., China) in the 0.3 to 20 A·g^{-1} current range, CV measurements were carried out on a BioLogic BCS-805 potentiostat (France) at a scan rate of 0.1 to 1.0 mV·s^{-1}. Electrochemical impedance spectroscopy (EIS) measurements were conducted in the 10 kHz-0.1 Hz frequency range at 1.4 V potential with 10 mV rms amplitude in a three-electrode electrochemical cell using a BioLogic BCS-805 potentiostat (France).

Results and discussion

The phase composition of the samples was determined by matching the XRD patterns (Figure 1) with the ICCD data. The initial powder peaks are well-resolved and correspond to the orthorhombic V_2O_5 (ICCD #01-077-2418). For the V-120 composite the XRD peaks match well with those of monoclinic $V_{10}O_{24}{\cdot}12H_2O$ (ICDD #00-025-1006). The peaks are broadened, indicating low crystallinity [32]. The most intense peak of the (0,0,2) plane at 6.48° allows to estimate the interlayer distance in $V_{10}O_{24}{\cdot}12H_2O$ as 1.36 nm. The indexable bands in the XRD pattern of sample V-170 correspond predominantly to those of monoclinic VO_2 (ICDD #01-084-3056).

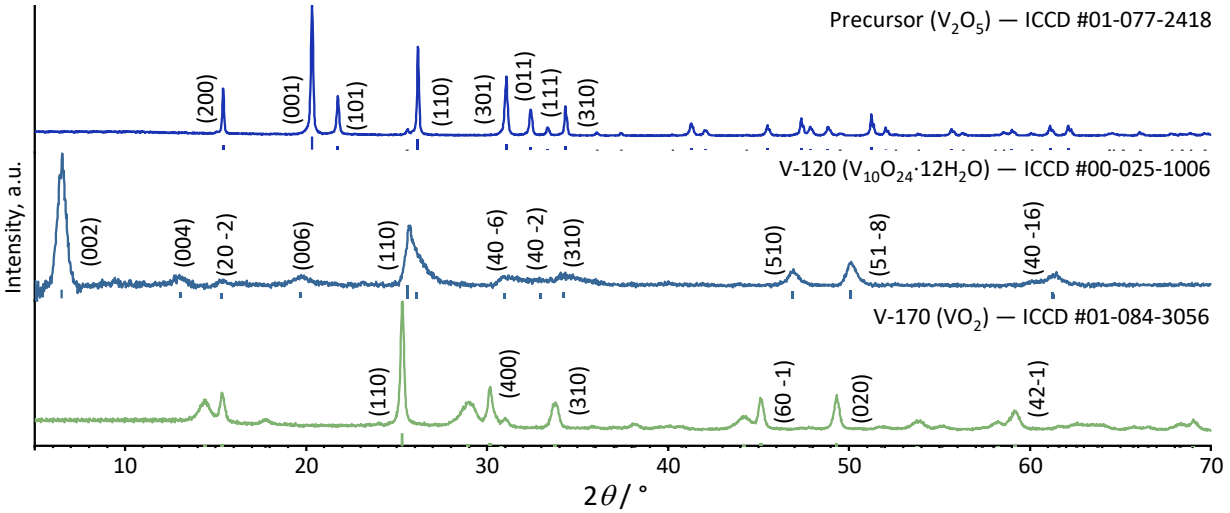

Figure 1. *XRD patterns of the powders of the initial V_2O_5 and composites V-120, V-170*

The XPS measurements were performed, and they showed the characteristic peaks of V, O, S, C elements. The XPS spectra of V 2p (Figure 2a) for both composites show the changes that occur with the vanadium oxide upon interaction with EDOT at different temperatures. Both V-120 and V-170 V 2p spectra contain the peaks at ~524.4 and ~526.0 eV for V $2p_{3/2}$ are related to V^{5+} and V^{4+}, respectively, which is consistent with available literature data [35]. The V $2p_{3/2}$-V $2p_{1/2}$ splitting value is 7.4 eV. The FWHM values for V $2p_{3/2}$ are ca. 1.4 eV, while the V $2p_{1/2}$ peaks are broadened, as the FWHM values are 2.57 eV, which is a result of the Coster-Kronig effect [36].

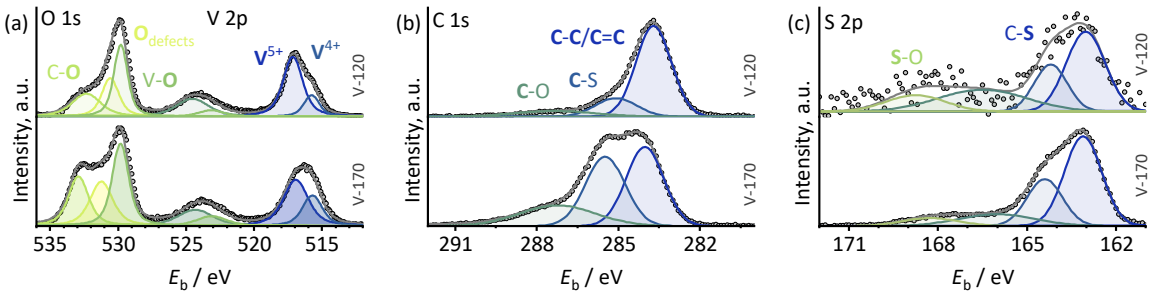

Figure 2. *XPS spectra of V-120 and V-170 samples in (a) O 1s and V 2p, (b) C 1s, and (c) S 2p regions*

There are three O 1s peaks present for both V-120 and V-170 samples (Figure 2a): the first one at 529.9 eV is typical [35] for oxygen in oxides and agrees well with the V 2p peaks. The second peak at a higher binding energy of 530.6-531.2 eV is related to the defective sites in the oxide crystal [37] and might overlap with C=O [38]. The third one at 532.3-532.9 eV we assign to the O-ether carbon atom signal due to the presence of PEDOT in the sample [39]. The trapped water can also provide this oxygen peak [40]. Since the oxidative polymerization occurs when the composite is formed by

the interaction of the initial V_2O_5 powder and the EDOT monomer, the reduction of the initial vanadium species should occur. From the XPS data, the V^{5+}/V^{4+} ratio for the composites can be estimated to be 3.5:1 for V-120 and 1.9:1 for V-170.

The XPS spectra of C 1s and S 2p (Figures 2b and 2c) further confirm the presence of PEDOT [41,42]. Specifically, the C 1s spectra contain three peaks: the most intense one at 283.9 eV is related to C-C/C=C, the peak at 285.2 eV is related to the C-S bond, and the one at 287.3 eV is for C-O, which is consistent with the O 1s spectra. Similar to O 1s, the intensity of the C 1s peak, which we attribute to the C-O bond, increases as the temperature of the synthesis increases. The S 2p spectra contain the peaks typical for the presence of S-O (166.4 and 168.8 eV) and C-S bonds (163.1 and 164.4 eV) [39] in the sample, which, along with the increase in the signal-to-noise ratio with increasing synthesis temperature, further confirms the formation of the V_2O_5/PEDOT composite.

The morphology of the samples was examined by SEM (Figures 3a and 3b). The V-120 sample consists of wavy layers with an average layer thickness of 0.6 to 1.0 µm. The V-170 sample consists of smaller needle-like crystals forming larger agglomerates. The EDX mapping (Figures 3c and 3d) for the S and V elements confirms the uniformity of their distribution and thus the rather complete coverage of V-120 and V-170 with PEDOT.

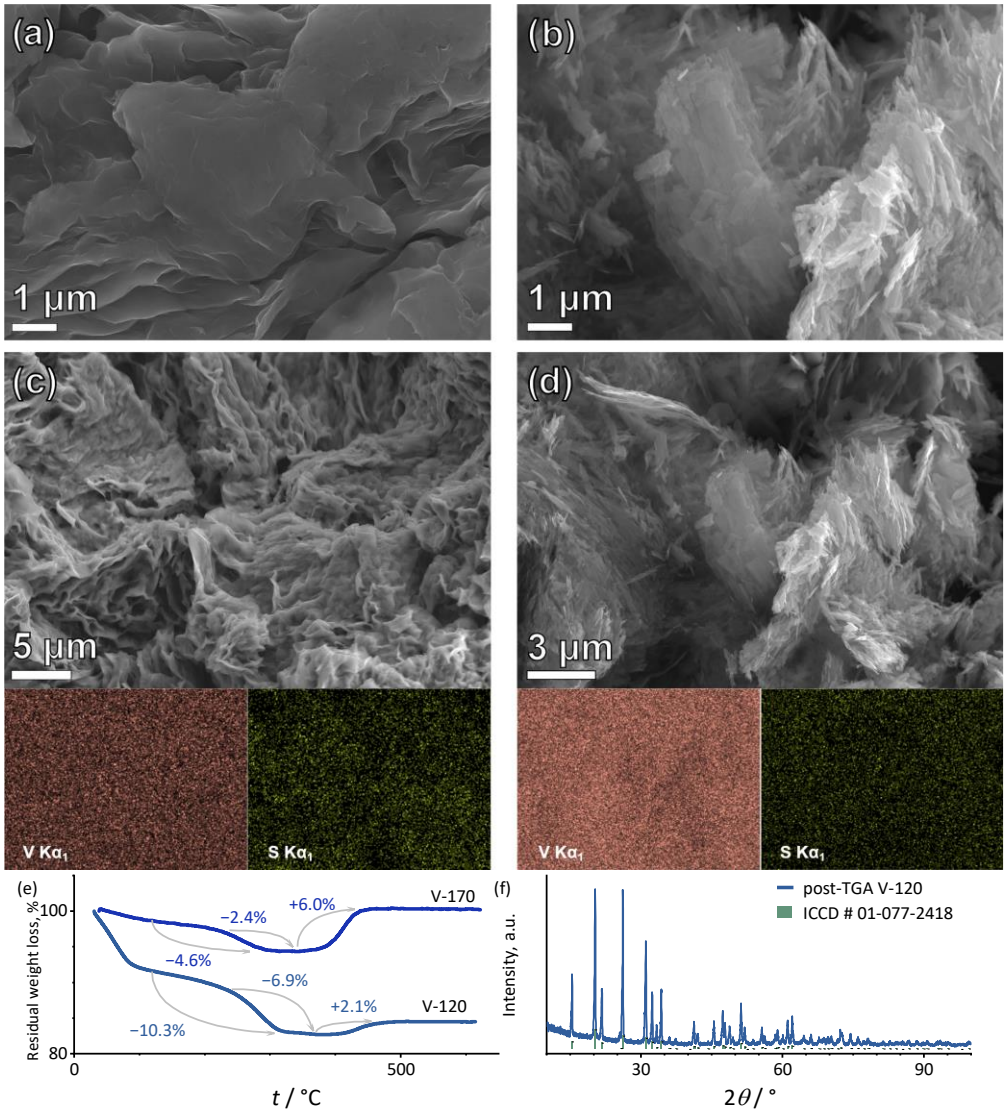

Figure 3. *SEM images of V-120 (a, c), and V-170 (b, d). SEM image with the corresponding EDX mapping of V and S elements for V-120 (c) and V-170 (d) samples, TGA curves for V-120 and V-170 samples (e), and XRD pattern of the V-120 sample after TGA (f)*

Thermogravimetric analysis in air (Figure 3f) allowed the determination of the PEDOT content in the V-120 and V-170 composites. The loss of moisture causes the initial weight decrease, which passes through two stages: the evaporation of free water, followed by the loss of interlayer water [40]. This is followed by the decomposition of PEDOT, with the most intense evaporation starting at 240 °C. The decomposition is completed at ~400 °C, and then the vanadium species in the V-120 and V-170 samples are oxidized to pristine orthorhombic V_2O_5, with oxygen uptake. This is confirmed by an XRD spectrum of the sample after thermogravimetric analysis (Figure 3g). As indicated by the TGA data, the PEDOT content in the composites was quite different. PEDOT constituted 2.4 % of the total weight in the V-170 sample, and 6.9 % in the case of V-120 sample.

Electrochemical performance

The CV of the V-120 sample (Figure 4a) contains two pairs of peaks at 0.76/0.63 and 1.09/0.96 V from the start. The same is true for V-170 (Figure 4b), for which the CV response contains two pairs of peaks at 0.73/0.59 V and 1.10/0.93 V. In both cases, the change in the positions of the peaks within ten cycles is insignificant. This contrasts with the evolution of the CV shape of the initial V_2O_5 which showed a drastic transformation of the current response during the ten cycles and structural transformations within the material structure [32]. During the same period, the more negative anodic peak in the V-170 voltammogram slightly decreases in intensity, while the more positive peak increases in intensity. Meanwhile, the cathodic peaks remain stable. For the V-120 electrode, there is no reorganization of the peaks in either intensity or position. Such behavior may be caused by V-120 having a more stable layered structure with large interlayer spacing, which allows for rapid Zn^{2+} (de)insertion.

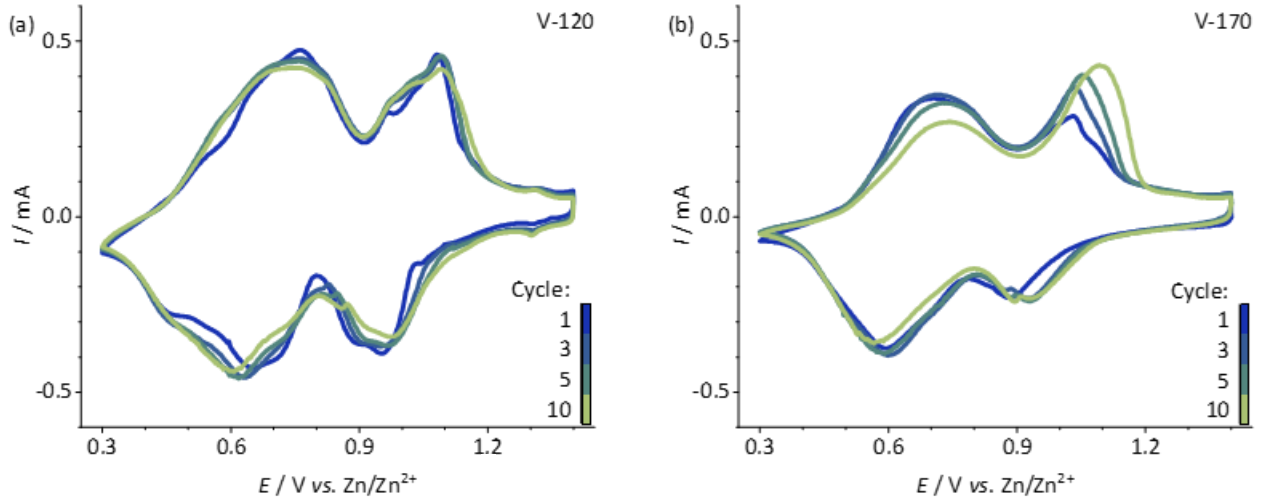

Figure 4. *CV curves of the initial ten cycles for the coin-cells with V-120 (a), V-170 (b) at a scan rate of 0.1 mV·s^{-1}*

The electrochemical performance of the electrode materials was also investigated by galvanostatic charge/discharge (Figure 5). The C-rate capability in asymmetric mode (with charge current of 0.3 A·g^{-1} and discharge current in the range of 0.3 to 20 A·g^{-1}) was studied for both electrodes (Figure 5a). For V-120, the discharge specific capacity values are 390, 357, 326, 274, 192, 137 and 101 mA·h·g^{-1} at current densities of 0.3, 1, 2, 5, 10, 15 and 20 A·g^{-1}. For V-170, the capacity values are 265, 207, 163, 108, 79, 60 and 46 mA·h·g^{-1} at the same current densities. The specific capacity values of V-120 exceed those of V-170 at every current density. V-170 provides similar specific capacity values to V_2O_5 at low current densities, yet V-170 prevails over V_2O_5 at high current densities, likely due to the facilitated kinetics of Zn^{2+} (de)intercalation [32].

Cycle life studies in symmetric charge/discharge mode at 2 $A \cdot g^{-1}$ (Figures 5b and 5c) show that the initial specific capacity of 215 $mA \cdot h \cdot g^{-1}$ of the V-120 sample increases continuously and reaches the maximum of 310 $mA \cdot h \cdot g^{-1}$ at the 175th cycle. The capacity then decreases until the final value of 228 $mA \cdot h \cdot g^{-1}$ is recorded. The capacity retention from the first cycle was 73.5 % of the maximum value. The specific capacity of V-170 is initially 215 $mA \cdot h \cdot g^{-1}$. This value decreases continuously and at the 1000th cycle only 100 $mA \cdot h \cdot g^{-1}$ remains, which is 46.5 % of the initial capacity. The cyclic stability of the materials in the symmetrical GCD mode at 5 $A \cdot g^{-1}$ is similar. Initially the V-120 sample provides the specific capacity value of 150 $mA \cdot h \cdot g^{-1}$. The capacity continues to increase until the 370th cycle, where the material provides 225 $mA \cdot h \cdot g^{-1}$. The next 630 cycles show a gradual decrease to 170 $mA \cdot h \cdot g^{-1}$. Again, the capacity retention exceeds 100 % of the initial value, yet the final capacity is 75.5 % of the maximum value. The initial specific capacity of 221 $mA \cdot h \cdot g^{-1}$ for V-170 falls rapidly, and the 1000th cycle has the capacity of only 26 $mA \cdot h \cdot g^{-1}$, which is 11.7 % of the initial value. The shapes of the GCD curves are typical of V_2O_5-based electrode materials. For V-120 and V-170 electrodes (Figures 5d and 5e), there is a pair of skewed intercalation-related plateaus in both the charge and discharge curves, although they diminish as the current rate increases. At high current densities, there is an almost-linear $E(Q)$ dependence, indicating a significant contribution from capacitive processes.

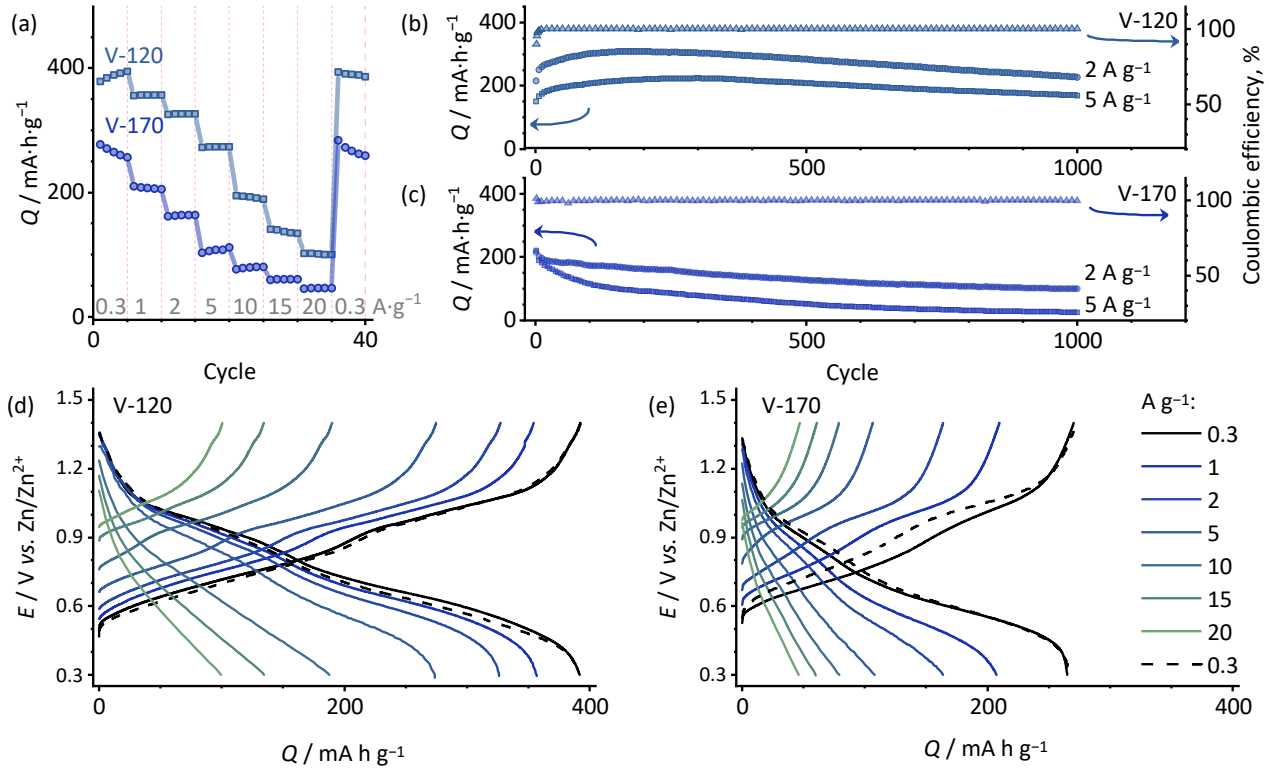

Figure 5. *C-rate performance and coulombic efficiency of V-120 and V-170 electrodes at currents from 0.3 $A \cdot g^{-1}$ to 20 $A \cdot g^{-1}$ (a); cycling performance and coulombic efficiency of electrodes V-120 (b) and V-170 (c) at currents of 2 $A \cdot g^{-1}$ and 5 $A \cdot g^{-1}$; charge/discharge curves for V-120 (d) and V-170 (e) from 0.3 $A \cdot g^{-1}$ to 20 $A \cdot g^{-1}$ (the dashed line is the return to 0.3 $A \cdot g^{-1}$ after all other currents)*

To estimate the contribution of diffusion-controlled and capacitive-controlled currents to the total measured currents, we performed CV measurements in the 0.3-1.4 V range at the scan rates from 0.1 to 1 $mV \cdot s^{-1}$ (Figures 6a and b). The shape of the CVs at different scan rates was similar for all electrode types, with a slight potential shift. The dependence of the peak current (i) on the scan rate (v) can be represented by (1):

$$i = a\,\nu^{b} \quad (1)$$

Or, in logarithmic form (2):

$$\log i = b \log \nu + \log a \quad (2)$$

Here the values *a* and *b* are constants. The constant *b* is usually in the 0.5 to 1.0 range, where the proximity to either 0.5 or 1.0 formally means that the current is controlled either by diffusion of the ions, or by capacitive processes, respectively.

Analysis of the rate dependence of the CV peaks (Figure 6c and 6d) for different materials shows that two redox peak pairs are dissimilar in their current contributions. This means that the currents of the process in the less positive potential region are diffusion-controlled, whereas capacitive control is prevalent for the redox processes at more positive potentials. The *b*-values for sample V-120 show this. We observed a significant contribution of capacitive processes over all redox peaks, with *b* = 0.85/0.88 for the less positive peak pair and *b* = 0.95/0.81 for the more positive one, which is usually typical of materials intended for use in supercapacitors [43]. The behavior of V-170 electrode is like that of the V_2O_5 electrode, as the more negative peak pair has *b* values of 0.61/0.72, *i.e.* the currents are diffusion-controlled, and the more positive has 0.90/0.80 values, indicating pseudocapacitive control. The predominant capacitive control of the current in the case of V-120 agrees well with the results reported for other V_2O_5-polymer composites [26,44-47].

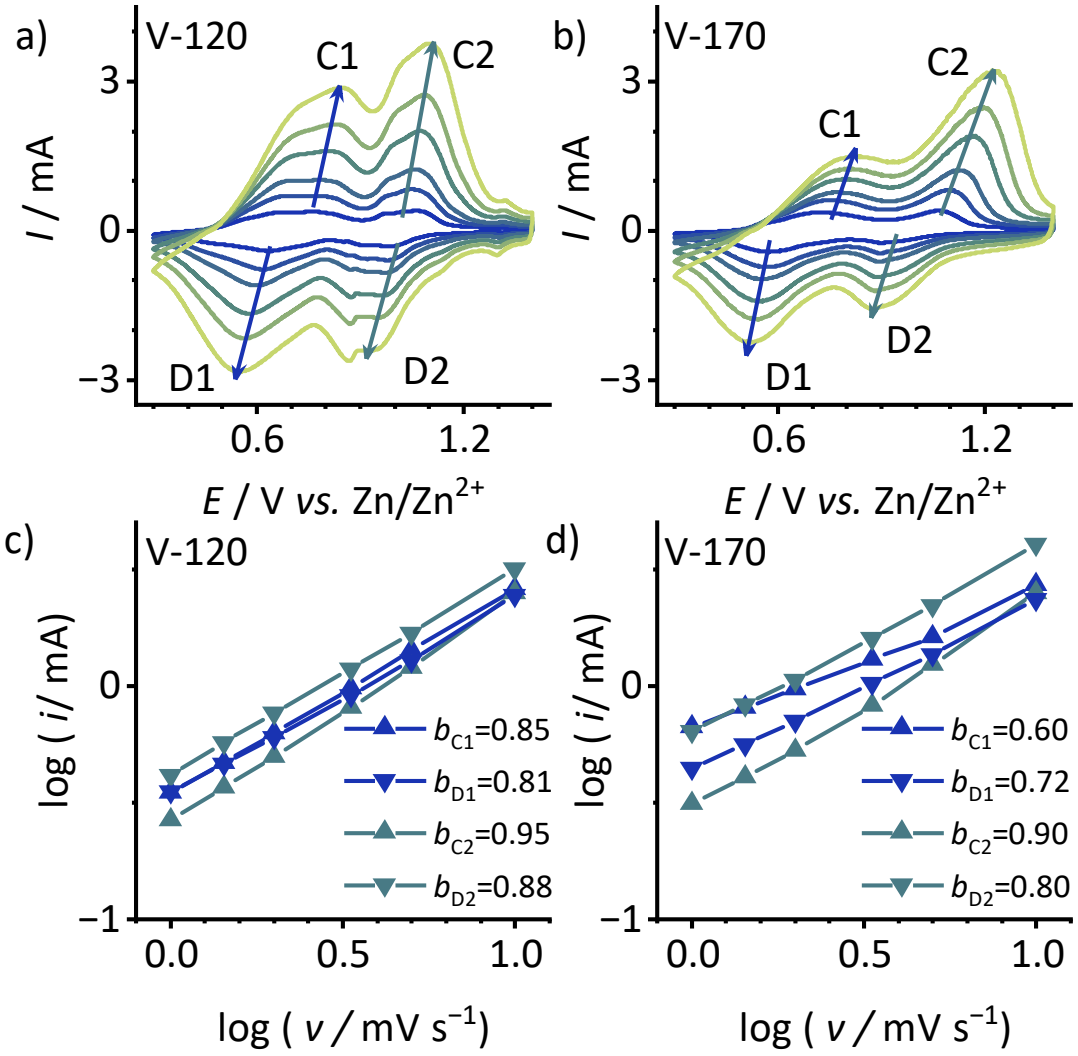

Figure 6. *CV curves for V-120 (a), V-170 (b) with different scan rates and log* i vs. *log* ν *curves of cathodic and anodic peaks of CV curves (c, d)*

The kinetics of the electrode processes was investigated by EIS in three-electrode cells with 3 mol·dm^{-3} $ZnSO_4$ electrolyte solution. The impedance spectra (Figure 7a) were recorded at 1.4 V after 10 GCD cycles at 0.1 A·g^{-1}. In the recorded spectra, the determined R_{ct} values were 2.2 Ω for V-120 and 9.8 Ω for V-170. Consistent with the reported enhanced capacity values, the V-120 electrode also has a lower R_{ct} value, which explains the facilitation of charge transport and hence can increase the capacity values of this material.

The presence of regions of 45° slope in the Nyquist plots for both samples indicate semi-infinite diffusion, modeled by Warburg impedance. This allows us to estimate Warburg constant values (σ_w) from the slopes of parallel linear sections in Z_{Re},$-Z_{Im}$ *vs.* $\omega^{-0.5}$ plots (Figure 7 b and 7c). For V-120 and V-170, σ_w equals 1.2 Ω·s$^{-0.5}$ and 1.7 Ω·s$^{-0.5}$, respectively. A slight difference shows that the apparent diffusion coefficients should also be within one order of magnitude, with V-120 having a slight advantage over the V-170 material.

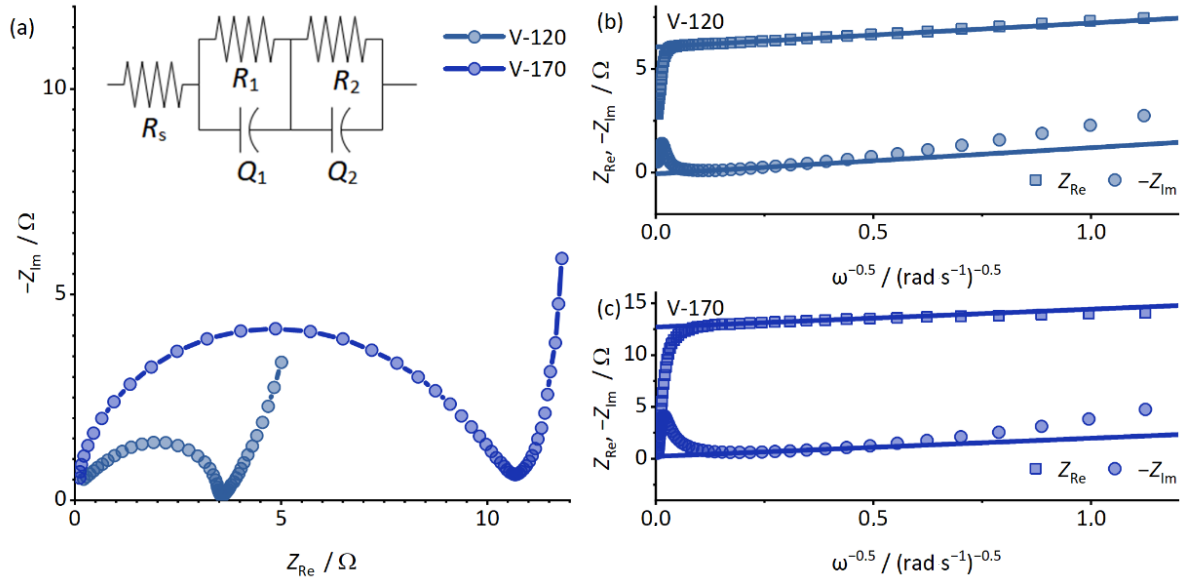

Figure 7. *Nyquist plots of EIS spectra of V-120 and V-170 electrodes in 10 kHz to 100 mHz range at 1.4 V (a),* Z_{Re},$-Z_{Im}$ vs. $\omega^{-0.5}$ *plots for V-120 (b) and V-170 (c) electrodes at 1.4 V with a linear fit of Warburg region,* i.e. *corresponding to the 45°-phase areas in Nyquist plots*

Conclusions

The vanadium oxide/poly(3,4-ethylenedioxythiophene) composites (V-120 and V-170) were successfully synthesized by a facile one-step microwave-assisted hydrothermal synthesis in two temperature modes at 120 and 170 °C, and their performance as cathodes in aqueous zinc-ion batteries was compared.

The obtained composites demonstrate excellent electrochemical performance, reaching specific capacities of up to 390 mA·h·g^{-1} at 0.3 A·g^{-1} (V-120) and maintaining the value of specific capacity 101 mA·h·g^{-1} at a high current density of 20 A·g^{-1}. In contrast to the pristine V_2O_5-based cathode, the activation process usually observed for such materials was negligible for both V-120 and V-170 materials.

The electrochemical properties of the composites based on vanadium oxide and PEDOT are therefore sensitive to the synthesis temperature. This is related to the difference in the results of the syntheses depending on the conditions: the composite samples synthesized at 170 °C contain both less structural water and PEDOT (2.4 vs. 6.9 % for V-120), which are responsible for the interlayer spacing and hence for the "lubrication" of Zn^{2+} diffusion. This could also result in lower

electronic and ionic conductivities of the composites, and thus a deterioration of the properties of the V-170 sample.

Acknowledgements: *The financial support from RFBR (grant № 21-53-53012) is gratefully acknowledged. The authors would like to thank the Centre for X-ray Diffraction Studies, the Interdisciplinary Resource Centre for Nanotechnology, the Centre for Physical Methods of Surface Investigation, the Thermogravimetric and Calorimetric Research Centre, the Chemical Analysis and Materials Research Centre and the Centre for Optical and Laser Materials Research of the Research Park of Saint Petersburg State University.*

Conflicts of Interest: *The authors declare no conflict of interest.*

References

[1] J. B. Goodenough, K. S. Park, The Li-ion rechargeable battery: A perspective, *Journal of the American Chemical Society* **135** (2013) 1167-1176. https://doi.org/10.1021/ja3091438

[2] M. Armand, P. Axmann, D. Bresser, M. Copley, K. Edström, C. Ekberg, D. Guyomard, B. Lestriez, P. Novák, M. Petranikova, W. Porcher, S. Trabesinger, M. Wohlfahrt-Mehrens, H. Zhang, Lithium-ion batteries - Current state of the art and anticipated developments, *Journal of Power Sources* **479** (2020) 228708. https://doi.org/10.1016/j.jpowsour.2020.228708

[3] D. Ouyang, M. Chen, Q. Huang, J. Weng, Z. Wang, J. Wang, A review on the thermal hazards of the lithium-ion battery and the corresponding countermeasures, *Applied Sciences* **9** (2019) 2483. https://doi.org/10.3390/app9122483

[4] J. Y. Hwang, S. T. Myung, Y. K. Sun, Sodium-ion batteries: Present and future, *Chemical Society Reviews* **46** (2017) 3529-3614 https://doi.org/10.1039/c6cs00776g

[5] K. Kubota, M. Dahbi, T. Hosaka, S. Kumakura, S. Komaba, Towards K-ion and Na-ion Batteries as "Beyond Li-Ion", *The Chemical Record* **18** (2018) 459-479. https://doi.org/10.1002/tcr.201700057

[6] J. Xie, Q. Zhang, Recent progress in multivalent metal (Mg, Zn, Ca, and Al) and metal-ion rechargeable batteries with organic materials as promising electrodes, *Small* **15** (2019) 1805061. https://doi.org/10.1002/smll.201805061

[7] Y. Liang, H. Dong, D. Aurbach, Y. Yao, Current status and future directions of multivalent metal-ion batteries, *Nature Energy* **5** (2020) 646-656. https://doi.org/10.1038/s41560-020-0655-0

[8] N. Borchers, S. Clark, B. Horstmann, K. Jayasayee, M. Juel, P. Stevens, Innovative zinc-based batteries, *Journal of Power Sources* **484** (2021) 229309. https://doi.org/10.1016/j.jpowsour.2020.229309

[9] H. Liu, J.G. Wang, Z. You, C. Wei, F. Kang, B. Wei, Rechargeable aqueous zinc-ion batteries: Mechanism, design strategies and future perspectives, *Materials Today* **42** (2021) 73-98. https://doi.org/10.1016/j.mattod.2020.08.021

[10] Y. Wu, T.Y. Song, L.N. Chen, A review on recent developments of vanadium-based cathode for rechargeable zinc-ion batteries, *Tungsten* **3** (2021) 289-304. https://doi.org/10.1007/s42864-021-00091-9

[11] G. Yang, Q. Li, K. Ma, C. Hong, C. Wang, The degradation mechanism of vanadium oxide-based aqueous zinc-ion batteries, *Journal of Materials Chemistry A* **8** (2020) 8084-8095. https://doi.org/10.1039/d0ta00615g

[12] X. Wang, Z. Zhang, B. Xi, W. Chen, Y. Jia, J. Feng, S. Xiong, Advances and perspectives of cathode storage chemistry in aqueous zinc-ion batteries, *ACS Nano* **15** (2021) 9244-9272. https://doi.org/10.1021/acsnano.1c01389

[13] J. Sun, Y. Zhao, Y. Liu, H. Jiang, C. Huang, M. Cui, T. Hu, C. Meng, Y. Zhang, "Three-in-one" strategy that ensures $V_2O_5 \cdot nH_2O$ with superior Zn^{2+} storage by simultaneous protonated polyaniline intercalation and encapsulation, *Small Structures* **3** (2022) 2100212. https://doi.org/10.1002/sstr.202100212

[14] W. Zhang, C. Zuo, C. Tang, W. Tang, B. Lan, X. Fu, S. Dong, P. Luo, The current developments and perspectives of V_2O_5 as cathode for rechargeable aqueous zinc-ion batteries, *Energy Technology* **9** (2021) 2000789. https://doi.org/10.1002/ente.202000789

[15] Y. Liu, X. Wu, Review of vanadium-based electrode materials for rechargeable aqueous zinc ion batteries, *Journal of Energy Chemistry* **56** (2021) 223-237. https://doi.org/10.1016/j.jechem.2020.08.016

[16] X. Zhang, X. Sun, X. Li, X. Hu, S. Cai, C. Zheng, Recent progress in rate and cycling performance modifications of vanadium oxides cathode for lithium-ion batteries, *Journal of Energy Chemistry* **59** (2021) 343-363. https://doi.org/10.1016/j.jechem.2020.11.022

[17] T.T. Lv, Y.Y. Liu, H. Wang, S.Y. Yang, C. Sen Liu, H. Pang, Crystal water enlarging the interlayer spacing of ultrathin $V_2O_5 \cdot 4VO_2 \cdot 2.72H_2O$ nanobelts for high-performance aqueous zinc-ion battery, *Chemical Engineering Journal* **411** (2021) 128533. https://doi.org/10.1016/j.cej.2021.128533

[18] M. Yan, P. He, Y. Chen, S. Wang, Q. Wei, K. Zhao, X. Xu, Q. An, Y. Shuang, Y. Shao, K.T. Mueller, L. Mai, J. Liu, J. Yang, Water-lubricated intercalation in $V_2O_5 \cdot nH_2O$ for high-capacity and high-rate aqueous rechargeable zinc batteries, *Advanced Materials* **30** (2018) 1703725. https://doi.org/10.1002/adma.201703725

[19] K. Zhu, T. Wu, K. Huang, Understanding the dissolution and phase transformation mechanisms in aqueous Zn/α-V_2O_5 batteries, *Chemistry of Materials* **33** (2021) 4089-4098. https://doi.org/10.1021/acs.chemmater.1c00715

[20] J. Shin, D.S. Choi, H.J. Lee, Y. Jung, J.W. Choi, Hydrated intercalation for high-performance aqueous zinc ion batteries, *Advanced Energy Materials* **9** (2019) 1900083. https://doi.org/10.1002/aenm.201900083

[21] T. Wu, K. Zhu, C. Qin, K. Huang, Unraveling the role of structural water in bilayer V_2O_5 during Zn^{2+}-intercalation: Insights from DFT calculations, *Journal of Materials Chemistry A* **7** (2019) 5612-5620. https://doi.org/10.1039/c8ta12014e

[22] R. Dong, T. Zhang, J. Liu, H. Li, D. Hu, X. Liu, Q. Xu, Mechanistic insight into polypyrrole coating on V_2O_5 cathode for aqueous zinc-ion battery, *ChemElectroChem* **9** (2022) 202101441. https://doi.org/10.1002/celc.202101441

[23] Y. Zhang, L. Xu, H. Jiang, Y. Liu, C. Meng, Polyaniline-expanded the interlayer spacing of hydrated vanadium pentoxide by the interface-intercalation for aqueous rechargeable Zn-ion batteries, *Journal of Colloid and Interface Science* **603** (2021) 641-650. https://doi.org/10.1016/j.jcis.2021.06.141

[24] R. Li, H. Zhang, J. Yan, Q. Zheng, X. Li, A novel 3-phenylpropylamine intercalated molecular bronze with ultrahigh layer spacing as a high-rate and stable cathode for aqueous zinc-ion batteries, *Fundamental Research* **1** (2021) 425-431. https://doi.org/10.1016/j.fmre.2021.06.017

[25] D. Xu, H. Wang, F. Li, Z. Guan, R. Wang, B. He, Y. Gong, X. Hu, Conformal conducting polymer shells on V_2O_5 nanosheet arrays as a high-rate and stable zinc-ion battery cathode, *Advanced Materials Interfaces* **6** (2019) 1801506. https://doi.org/10.1002/admi.201801506

[26] X. Liu, G. Xu, Q. Zhang, S. Huang, L. Li, X. Wei, J. Cao, L. Yang, P.K. Chu, Ultrathin hybrid nanobelts of single-crystalline VO_2 and poly(3,4-ethylenedioxythiophene) as cathode materials for aqueous zinc ion batteries with large capacity and high-rate capability, *Journal of Power Sources* **463** (2020) 228223. https://doi.org/10.1016/j.jpowsour.2020.228223

[27] D. Bin, W. Huo, Y. Yuan, J. Huang, Y. Liu, Y. Zhang, F. Dong, Y. Wang, Y. Xia, Organic-inorganic-induced polymer intercalation into layered composites for aqueous zinc-ion battery, *Chem* **6** (2020) 968-984. https://doi.org/10.1016/j.chempr.2020.02.001

[28] W. Bi, G. Gao, G. Wu, M. Atif, M. S. AlSalhi, G. Cao, Sodium vanadate/PEDOT nanocables rich with oxygen vacancies for high energy conversion efficiency zinc ion batteries, *Energy Storage Materials* **40** (2021) 209-218. https://doi.org/10.1016/j.ensm.2021.05.003

[29] Y. Du, X. Wang, J. Man, J. Sun, A novel organic-inorganic hybrid V_2O_5@polyaniline as high-performance cathode for aqueous zinc-ion batteries, *Materials Letters* **272** (2020) 127813. https://doi.org/10.1016/j.matlet.2020.127813

[30] Z. Zhang, B. Xi, X. Wang, X. Ma, W. Chen, J. Feng, S. Xiong, Oxygen defects engineering of $VO_2{\cdot}xH_2O$ nanosheets via in situ polypyrrole polymerization for efficient aqueous zinc ion storage, *Advanced Functional Materials* **31** (2021) 2103070. https://doi.org/10.1002/adfm.202103070

[31] H. Ling, R. Zhang, X. Ye, Z. Wen, J. Xia, X. Lu, In-situ synthesis of organic-inorganic hybrid thin film of PEDOT/V_2O_5 as hole transport layer for polymer solar cells, *Solar Energy* **190** (2019) 63-68. https://doi.org/10.1016/j.solener.2019.07.095

[32] F.S. Volkov, E.G. Tolstopjatova, S.N. Eliseeva, M.A. Kamenskii, A.I. Vypritskaia, A.I. Volkov, V. V. Kondratiev, Vanadium(V) oxide coated by poly(3,4-ethylenedioxythiophene) as cathode for aqueous zinc-ion batteries with improved electrochemical performance, *Materials Letters* **308** (2022) 131210. https://doi.org/10.1016/j.matlet.2021.131210

[33] F.S. Volkov, S.N. Eliseeva, M.A. Kamenskii, A.I. Volkov, E.G. Tolstopjatova, O. V. Glumov, L. Fu, V. V. Kondratiev, Vanadium oxide-poly(3,4-ethylenedioxythiophene) nanocomposite as high-performance cathode for aqueous Zn-ion batteries: The structural and electrochemical characterization, *Nanomaterials* **12** (2022) 3896. https://doi.org/10.3390/nano12213896

[34] A. V. Murugan, C. W. Kwon, G. Campet, B. B. Kale, A. B. Mandale, S. R. Sainker, C. S. Gopinath, K. Vijayamohanan, A novel approach to prepare poly(3,4-ethylenedioxythiophene) nanoribbons between V_2O_5 layers by microwave irradiation, *Journal of Physical Chemistry B* **108** (2004) 10736-10742. https://doi.org/10.1021/jp048859g

[35] M. C. Biesinger, B. P. Payne, A. P. Grosvenor, L. W. M. Lau, A. R. Gerson, R. S. C. Smart, Resolving surface chemical states in XPS analysis of first row transition metals, oxides and hydroxides: Cr, Mn, Fe, Co and Ni, *Applied Surface Science* **257** (2011) 2717-2730. https://doi.org/10.1016/j.apsusc.2010.10.051

[36] G. Silversmit, D. Depla, H. Poelman, G.B. Marin, R. De Gryse, An XPS study on the surface reduction of V_2O_5(0 0 1) induced by Ar^+ ion bombardment, *Surface Science* **600** (2006) 3512-3517. https://doi.org/10.1016/j.susc.2006.07.006

[37] M. C. Biesinger, B. P. Payne, L. W. M. Lau, A. Gerson, R. S. C. Smart, X-ray photoelectron spectroscopic chemical state quantification of mixed nickel metal, oxide and hydroxide systems, *Surface and Interface Analysis* **41** (2009) 324-332. https://doi.org/10.1002/sia.3026

[38] S. Reddy, Q. Xiao, H. Liu, C. Li, S. Chen, C. Wang, K. Chiu, N. Chen, Y. Tu, S. Ramakrishna, L. He, Bionanotube/poly(3,4-ethylenedioxythiophene) nanohybrid as an electrode for the neural interface and dopamine sensor, *ACS Applied Materials and Interfaces* **11** (2019) 18254-18267. https://doi.org/10.1021/acsami.9b04862

[39] E. Mitraka, M. J. Jafari, M. Vagin, X. Liu, M. Fahlman, T. Ederth, M. Berggren, M. P. Jonsson, X. Crispin, Oxygen-induced doping on reduced PEDOT, *Journal of Materials Chemistry A* **5** (2017) 4404-4412. https://doi.org/10.1039/C6TA10521A

[40] H. Chen, J. Huang, S. Tian, L. Liu, T. Qin, L. Song, Y. Liu, Y. Zhang, X. Wu, S. Lei, S. Peng, Interlayer modification of pseudocapacitive vanadium oxide and $Zn(H_2O)_n^{2+}$ migration

regulation for ultrahigh rate and durable aqueous zinc-ion batteries, *Advanced Science* **8** (2021) 2004924. https://doi.org/10.1002/advs.202004924

[41] A. Et Taouil, F. Lallemand, J. Y. Hihn, J. M. Melot, V. Blondeau-Patissier, B. Lakard, Doping properties of PEDOT films electrosynthesized under high frequency ultrasound irradiation, *Ultrasonics Sonochemistry* **18** (2011) 140-148. https://doi.org/10.1016/j.ultsonch.2010.04.003

[42] G. Beamson, D. Briggs, *High Resolution XPS of Organic Polymers: The Scienta ESCA300 Database*, Wiley, 1992. ISBN 9780471935926

[43] W. Zong, H. Guo, Y. Ouyang, L. Mo, C. Zhou, G. Chao, J. Hofkens, Y. Xu, W. Wang, Y. E. Miao, G. He, I. P. Parkin, F. Lai, T. Liu, Topochemistry-driven synthesis of transition-metal selenides with weakened van der Waals force to enable 3D-printed Na-ion hybrid capacitors, *Advanced Functional Materials* **32** (2022) 2110016. https://doi.org/10.1002/adfm.202110016

[44] H. Yan, Q. Ru, P. Gao, Z. Shi, Y. Gao, F. Chen, F. Chi-Chun Ling, L. Wei, Organic pillars pre-intercalated V^{4+}-$V_2O_5{\cdot}3H_2O$ nanocomposites with enlarged interlayer and mixed valence for aqueous Zn-ion storage, *Applied Surface Science* **534** (2020) 147608. https://doi.org/10.1016/j.apsusc.2020.147608

[45] Z. Feng, J. Sun, Y. Liu, H. Jiang, T. Hu, M. Cui, F. Tian, C. Meng, Y. Zhang, Polypyrrole-intercalation tuning lamellar structure of $V_2O_5{\cdot}nH_2O$ boosts fast zinc-ion kinetics for aqueous zinc-ion battery, *Journal of Power Sources* **536** (2022) 231489. https://doi.org/10.1016/j.jpowsour.2022.231489

[46] S. Li, X. Wei, C. Wu, B. Zhang, S. Wu, Z. Lin, Constructing three-dimensional structured V_2O_5/conductive polymer composite with fast ion/electron transfer kinetics for aqueous zinc-ion battery, *ACS Applied Energy Materials* **4** (2021) 4208-4216. https://doi.org/10.1021/acsaem.1c00573

[47] R. Li, F. Xing, T. Li, H. Zhang, J. Yan, Q. Zheng, X. Li, Intercalated polyaniline in V_2O_5 as a unique vanadium oxide bronze cathode for highly stable aqueous zinc ion battery, *Energy Storage Materials* **38** (2021) 590-598. https://doi.org/10.1016/j.ensm.2021.04.004